PCCP

Accepted Manuscript




ROYAL SOCIETY OF CHEMISTRY

www.rsc.org/pccp

Physical Chemistry Chemical Physics
CREATED USING THE RSC LaTeX PCCP ARTICLE TEMPLATE – SEE www.rsc.org/electronicfiles FOR DETAILS
ARTICLE TYPE www. rsc.org/xxxxxx | XXXXXXXX

# Electronic state dependence of heterogeneous electron transfer: Injection from the $S_1$ and $S_2$ state of phlorin into $TiO_2$

**Jesus Nieto-Pescador,[a] Baxter Abraham,[b] Allen J. Pistner,[b] Joel Rosenthal,[b] and Lars Gundlach*[a,b]**

***Received Xth XXXXXXXXXX 20XX, Accepted Xth XXXXXXXXX 20XX***
***First published on the web Xth XXXXXXXXXX 200X***
**DOI: 10.1039/b000000x**

Ultrafast time-resolved measurements were performed on a novel pentafluorophenyl substituted 5,5-dimethyl phlorin derivative in solution and when attached to $TiO_2$ colloidal films. The complex excited state dynamics of this porphyrinoid after $S_1$ and $S_2$ excitation was compared at different wavelengths and can be assigned to several subsequent relaxation mechanisms. The difference between excited state dynamics in the free molecule and when attached to an electron accepting electrode was measured. For both cases the dynamics was compared after excitation to the $S_1$ and the $S_2$ state. For the free molecule in solution an intermediate relaxation step was identified and assigned to a buckling motion of the tetrapyrrole ring. On the electrode, heterogeneous electron transfer (HET) times from both states were very similar and around 50 fs. Surprisingly, the large difference in the density of acceptor states that are resonant with the respective donor level of the molecule does not significantly influence HET dynamics. This result indicates that HET proceeds into intermediate transition states that are different from steady state surface states obtained from experiments or computations. The density of states (DOS) of these transient acceptor states appears not to be directly related to the corresponding surface or bulk DOS.

## 1 Introduction

Utilizing sunlight for energy production requires a light absorbing material. In the case of molecular absorbers, e.g. organic or organometallic molecules, light absorption is followed by charge redistribution. This occurs regardless of whether light is directly transformed into electric current or used to drive chemical reactions for generating solar fuels. The two main challenges for designing suitable molecules are their ability to absorb as much of the solar spectrum as possible and to keep the converted energy in a state where it can either be used to drive a chemical reaction or charge separation in a solar cell. Porphyrins have attracted much attention as sensitizers for dye-sensitized solar cells (DSSCs) as well as for photocatalytic applications.[1–6] Recently, a fluorinated free-base porphyrinoid has been synthesized that showed multi-electron redox reaction capability[7,8] and enhanced absorption in the red spectral region as a potential photosensitizer in a DSSC. Many porphyrinoids show interesting photophysics due to a strong $S_0 \rightarrow S_2$ transition dipole moment followed by a very rapid $S_2 \rightarrow S_1$ internal conversion (IC). Excited state dynamics of porphyrins have been measured in real time in solution,[9–11] and attached to different metal oxide semiconductors.[5,12,13] A special property of porphyrinoids is that they allow for comparing dynamics for different excitation energies. Measurements comparing excited state dynamics starting from the $S_1$ state and the $S_2$ state have been performed in solution phase on free base TPP,[9] on Zn-TTP,[10] and on a Zn-bisporphyrin.[11]

In this work we investigate excited state dynamics of a phlorin macrocycle in solution and when attached to $TiO_2$ nanoparticles after $S_1$ and $S_2$ excitation. Comparing heterogeneous electron transfer (HET) dynamics from the $S_1$ and $S_2$ state is especially interesting because it constitutes the rare case where the excess energy of the electron donating molecular state can be varied without any changes to the samples. With this, it is possible to investigate the influence of the density of acceptor states on electron transfer (ET) dynamics. The phlorin derivative investigated here is especially suited for this study because it shows strongly enhanced absorption in the Q-band ($S_1$ state), which for most simple porphyrins is 20 to 30 times smaller than the absorption of the Soret band. Thus, phlorin derivatives such as those shown in Fig. 1 allow to compare injection from both states without the need for major changes in excitation fluence or concentration of molecules. Before we discuss HET dynamics of the bound molecule, we examine excited state dynamics in solution phase in order to distinguish between intra molecular dynamics and HET dynamics.

[a] *Department of Physics and Astronomy, University of Delaware, Newark, DE 19716 USA.*
[b] *Department of Chemistry and Biochemistry, University of Delaware, Newark, DE 19716 USA. E-mail: larsg@udel.edu*

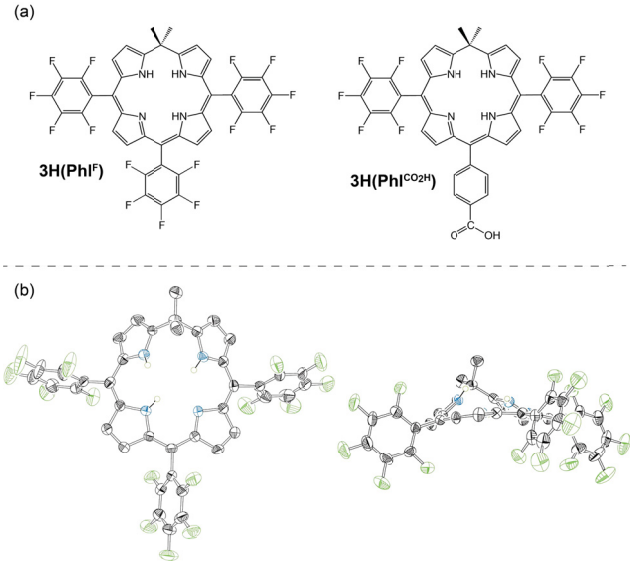


**Fig. 1** (a) Freebase phlorin derivatives utilized in this study. (b) Solid state structure of 3H(Phl$^F$) shown from above the plane of the macrocycle (left) and side one (right). A molecule of cocrystallized $CHCl_3$ and all non-nitrogen bound hydrogen atoms have been omitted for clarity.

## 2 Experimental section

### 2.1 Apparatus.

Steady state absorption and fluorescence were recorded with a HP-8452A spectrophotometer and a PTI Quantamaster-300 spectrofluorometer, respectively. Transient differential absorbance measurements were performed using standard methods which are described below.[14,15] A Ti:Saphire oscillator (Coherent Mantis) seeded a regenerative amplifier (Coherent Legend-Elite) producing a train of 35 fs pulses centered at 800 nm with a repetition rate of 10 kHz and 620 μJ of energy. A fraction of the amplifier output (120 μJ) was used to pump a home built non-collinear parametric amplifier (NOPA) that delivers sub 30 fs pulses after compression. The NOPA was either tuned to 650 nm for excitation in the Q-band or to 880 nm to generate 440 nm pump pulses after second harmonic generation in a 0.1 mm BBO crystal. The supercontinuum probe was generated by focusing 0.1 μJ in a 3 mm thick sapphire window followed by compression by a pair of BK7 prisms. The pump beam path included a motorized delay stage, a chopper wheel, and a half wave-plate. Pump and probe beams were focused onto the sample using a parabolic mirror resulting in a spot diameter of 350 μm for the pump and a fluence of 311 μJ/cm$^2$. The probe beam diameter was always below 100 μm. After the sample, the probe beam was spatially filtered and sent through a beam splitter. One arm was chopped and recombined with the second arm before entering the monochromator for a ratiometric measurement. Finally, the signal was detected after the monochromator (Oriel Cornerstone 260) with a biased Si photodiode (Thorlabs DET10A) and measured differentially with a dual reference lock-in amplifier (Signal Recovery 7230 DSP).

### 2.2 Measurement procedure.

Two different procedures were performed: one for recording kinetic traces, another for obtaining the transient spectral response.

**2.2.1 Kinetic trace measurements.** After compressing both beams, the pump beam was cross-correlated with the desired part of the supercontinuum probe in a 0.2 mm BBO crystal. A Gaussian fit to the correlation signal was used as the instrument response function (IRF). Typical values for the full width at half maximum (FWHM) of the IRF were around 33 to 65 fs, depending on the probe wavelength; generally a narrower IRF was attained at shorter wavelengths. It is important to note that with the fitting procedure, described later, it is possible to resolve time constants shorter than the IRF (*i.e.* ∼20 fs).[16] After measuring the IRF the crystal was replaced by a 1 mm optical length cuvette or a vacuum chamber containing the film sample (base pressure $10^{-7}$ mbar). The concentration of the sample and the intensity of the pump beam were varied respectively to ensure all measurements were performed in regions of linear response. Additionally, to check the strength of any coherent artifact present in the signal, a measurement from a cell filled only with solvent was recorded as part of our measurements. Contributions from the artifact was minimized by changing the position of the focus within the cell. All measurements in solution were performed with the polarizations adjusted to magic angle.

**2.2.2 Transient spectra measurements.** First, the supercontinuum probe was compressed to minimize the IRF resulting in 35 to 80 fs in the range of 500-720 nm. The dispersion of the supercontinuum was characterized by cross-correlation with the pump beam in BBO.[17] The temporal profile was fitted using a polynomial function and was used as a time correction during the data acquisition. Measurements were performed by setting the dual reference lock-in amplifier to record the ratio of the two signals chopped at different frequencies: differential absorption and probe intensity. Although the described procedure was carefully followed, the acquired transient spectra do not have the same time resolution as the kinetic traces. This is due to the fact that pulse compression can only be optimized for limited wavelength range with our method. Consequently, the spectral profiles are primarily used to gain general insight into the ongoing processes, while time-dependent parameters were extracted from the higher time resolution kinetic traces.

### 2.3 Phlorin synthesis.

**2.3.1 Synthetic materials and methods.** Reactions were performed in oven-dried round-bottomed flasks unless otherwise noted. Reactions that required an inert atmosphere were conducted under a positive pressure of $N_2$ using flasks fitted with Suba-Seal rubber septa or in a nitrogen filled glove box. Air and moisture sensitive reagents were transferred using standard syringe or cannula techniques. Reagents and solvents were purchased from Sigma Aldrich, Acros, Fisher, Strem, or Cambridge Isotopes Laboratories. Solvents for synthesis were of reagent grade or better and were dried by passage through activated alumina and then stored over 4 Å molecular sieves prior to use. Phlorin derivatives 3H($\mathrm{Phl^F}$) and 3H($\mathrm{Phl^{CO_2tBu}}$) were prepared using previously described methods.[7,18] Fig. 1 illustrates the phlorins employed in this study along with the solid state structure of 3H($\mathrm{Phl^F}$), which was previously obtained by X-ray diffraction.[18] All other reagents were used as received.

**2.3.2 Compound characterization.** $^1$H NMR and $^{13}$C NMR spectra were recorded at 25 °C on a Bruker 400 MHz spectrometer. Proton spectra are referenced to the residual proton resonance of the deuterated solvent ($CD_3CN$ = $\delta$ 1.94). All chemical shifts are reported using the standard $\delta$ notation in parts-per-million; positive chemical shifts are to higher frequency from the given reference. LR-GCMS data were obtained using an Agilent gas chromatograph consisting of a 6850 Series GC System equipped with a 5973 Network Mass Selective Detector. LR-ESI MS data was obtained using either a LCQ Advantage from Thermofinnigan or a Shimadzu LCMS-2020. High-resolution mass spectrometry analyses were performed by the Mass Spectrometry Laboratory in the Department of Chemistry and Biochemistry at the University of Delaware.

**2.3.3 5,5-Dimethyl-10,20-bis(pentafluorophenyl)-15-(4-carboxyphenyl)phlorin (3H($\mathrm{Phl^{CO_2H}}$)).** To a solution of 3H($\mathrm{Phl^{CO_2tBu}}$) (100 mg, 0.125 mmol) dissolved in 40 mL of dichloromethane was added 745 µL of trifluoroacetic acid (10 mmol). This reaction solution was stirred at room temperature for 12 hrs under air. Following removal of the solvent under reduced pressure, the reaction mixture was purified by chromatography on silica using $CH_2Cl_2$ and $CH_3OH$ (50:1) as the eluent. The crude product was subjected to a second chromatographic step using a silica column with a mobile phase comprised of hexanes and ethyl acetate (1:1) to deliver 47 mg of the title compound as a green solid in 50% yield. $^1$H NMR (400 MHz, $CD_3CN$) $\delta$/ppm: 8.17 (d, J = 8.2 Hz, 2H), 7.78 (d, J = 8.2 Hz, 2H), 7.45 (d, J = 5.0 Hz, 2H), 7.27 (d, J = 5.1 Hz, 2H), 7.00 (d, J = 3.8 Hz, 2H), 6.81 (d, J = 3.9 Hz, 2H), 1.51 (s, 6H). HR-ESI-MS $[M+H]^+$ m/z: calc for $C_{41}H_{23}N_4O_2F_{10}$, 793.1661; found, 793.1663.

### 2.4 Sample preparation.

Experiments in solution were performed using spectroscopy grade methanol and reagent grade toluene, dimethylformamide (DMF), and cyclohexane from Fisher Scientific. For the sensitized film measurements, nanoporous anatase $TiO_2$ films were prepared in two steps. First, the colloidal $TiO_2$ solution was synthesized by hydrolysis of Ti(IV)−isopropylate and autoclaving of the acidified sol; the sol-gel technique is described elsewhere.[19] Next, the colloidal solution was cast onto 50 µm thin AF45 glass (Schott Displayglas) via doctor blading. This method resulted in mesoporous films of ∼10 µm thickness consisting of nanoparticles with an average diameter of ∼20 nm.

**2.4.1 Sensitization procedure.** Nanoporous anatase $TiO_2$ films were sensitized using the following method. Firstly, a $TiO_2$ thin film was annealed in a furnace at 450 °C. Next, the film was immersed in a 100 µM solution of 3H($\mathrm{Phl^{CO_2H}}$) in toluene for about 45 min. Afterward, the dye-covered film was rinsed in pure solvent and blown dry with argon. Finally, the sensitized film was quickly placed in a vacuum chamber with a 0.5 mm fused silica window at $10^{-7}$ mbar.

Photobleaching of porphyrin samples in solutions has been reported after excitation at 397 nm.[10] Pumping at the absorption maximum around 440 nm reduced photobleaching and allowed for employing relatively low excitation fluences. Solution phase measurements were performed without employing a flow cell since convection was sufficient for replenishing the sample. For film measurements a reduction of the transient absorption signal during the first 20 min of irradiation was observed. This was accompanied by a bleach of the sample. Similar photobleaching has been observed earlier[20] and has been ascribed to photo-oxidation of unbound molecules in the film that reside in a photoexcited, highly reactive state for a prolonged time. Properly bound molecules, on the other hand, undergo rapid ET transfer resulting in the molecular cation. The UHV environment slowed down the photobleach process and allowed for comparing measurements at the beginning and the end of this process. No change in the absorption, emission spectra or dynamics was observed. All measurements were performed after an initial 30 min bleach period. It should be noted that the 440 nm pump pulse does not provide sufficient energy for interband transitions in $TiO_2$.

### 2.5 Analysis procedure.

Measured transient signals at different wavelengths, $\sigma_\lambda$, were fitted to the expression

$$\sigma_\lambda(t) = \sum_{i=0}^{n} A_i^\lambda N_i(t), \quad (1)$$

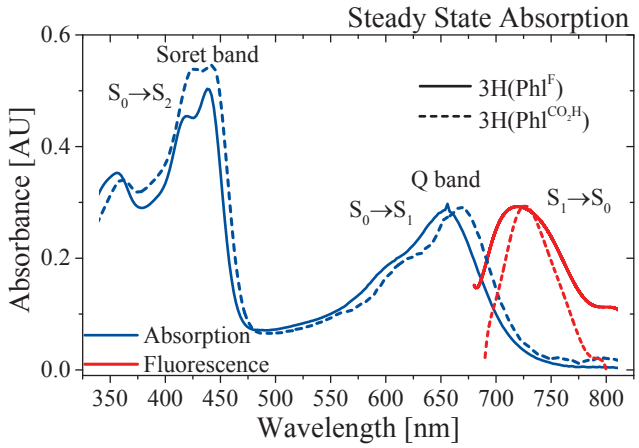


**Fig. 2** The ground state absorption and static fluorescence spectra of 3H(Phl$^{F}$) and 3H(Phl$^{CO_2H}$) in toluene.

where $A_i^{\lambda}$ represents the independent amplitude at each wavelength and $N_i(t)$ the population in a given state. The $n$ number of terms in equation 1 represent the states involved in the relaxation process. Hence, the number $n$ was kept at the minimum to fit the signal at all wavelengths, using the same number of states, without having any systematic deviation of the fit residuals. The signal at a given wavelength has a weighted contribution of the population from all states involved.

The time dependent populations of each state were obtained by solving the following set of linear rate equations:

$$\dot{N}_0(t) = -Bg(t) + \frac{1}{\tau_n} N_n(t), \quad (2)$$

$$\dot{N}_1(t) = Bg(t) - \frac{1}{\tau_1} N_1(t), \quad (3)$$

$$\dot{N}_i(t) = \frac{1}{\tau_{i-1}} N_{i-1}(t) - \frac{1}{\tau_i} N_i(t), \quad (4)$$

where $\tau_i$ are decay parameters associated at each state. The term $Bg(t)$ in (2) acts as a source for the population originating from the pump pulse and is composed of an amplitude $B$ and Gaussian envelope $g(t)$. The envelope

$$g(t) = \exp\left[-4\ln(2)\left(\frac{t-t_0}{\mathscr{F}_{IRF}}\right)^2\right] \quad (5)$$

takes in to account $\mathscr{F}_{IRF}$ as the full width at half maximum of our IRF. The objective of the fitting routine is therefore to find the set of parameters $\{A_i^{\lambda}, \tau_i\}$ that results in the best global fit.

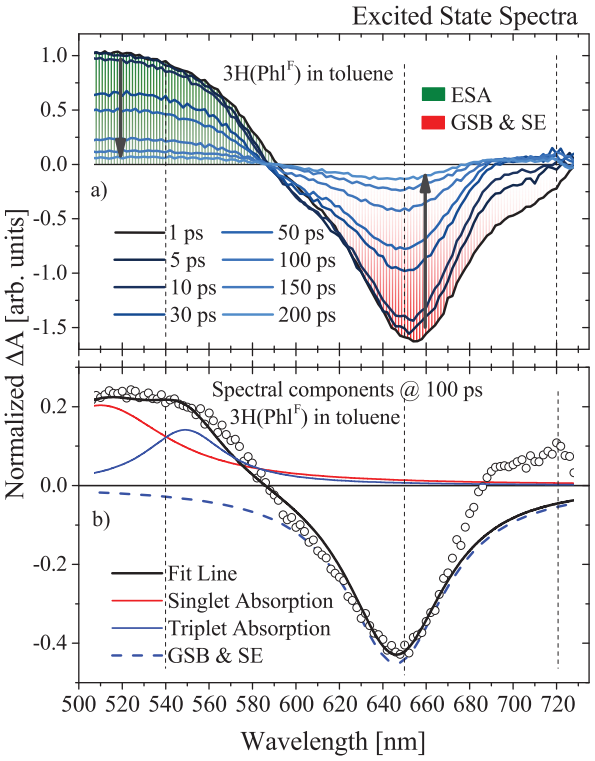


**Fig. 3** Normalized absorbance difference spectra at different delay times following Soret band excitation. Dashed lines show the wavelengths at which kinetic traces were taken.

## 3 Results and Discussions

### 3.1 Steady-state measurements.

Ground state absorption and emission spectra of 3H(Phl$^{F}$) and 3H(Phl$^{CO_2H}$) are shown in Fig. 2 and agree with previously reported measurements on phlorins.[7,21] The phlorin, being a porphyrinoid, absorbs light with a Soret band at ~440 nm and in the Q band at ~650 nm. These absorption bands correspond to the $S_0 \rightarrow S_2$ and $S_0 \rightarrow S_1$ transitions, respectively . The emission spectra show a Stokes shift to ~730 nm. The acid form of the phlorin shows a slight red shift of the Q band and consequently a shift in the emission spectra. It is worth noting that according to Gouterman's four orbital model of porphyrins,[22] the reduction of symmetry in the phlorin compared to standard porphyrins accounts for the degeneracy of the $Q_x$ and $Q_y$ bands. Due to this fact, all processes in the singlet excited state $S_1$, will be attributed to the Q band without making further distinctions.

### 3.2 Transient absorption of phlorin in solution.

**3.2.1 Spectroscopic properties.** Transient absorption spectra after excitation of the Soret band are shown in Fig. 3.

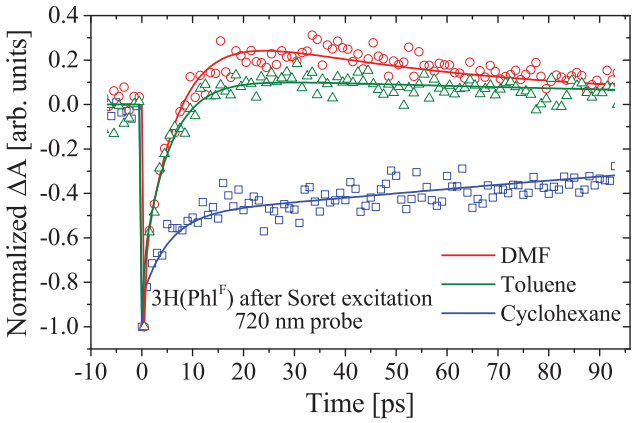


**Fig. 4** Comparison of the relaxation dynamics of 3H(Phl$^{F}$) for different solvents. Solid lines represent the fit.

There are several notable features in these spectra. One is a positive peak with a maximum around 510 nm assigned to a mixture of two contributions. The first contributor is the early singlet excited state absorption (ESA) $S_1 \rightarrow S_n$, similarly observed in previous porphyrin studies.[23–26] The peak evolves to a weak absorption plateau after ~50 ps which is assigned to absorption in the triplet state $T_1 \rightarrow T_n$. Similar absorption from the triplet state has been previously reported in theoretical and experimental studies.[26–28] There exists an isosbestic point at 590 nm separating the absorption signal from a peak with negative signal centered at 650 nm. The negative signal is a mixed contribution of ground state bleach (GSB) and stimulated emission (SE). Consequently, the short wavelength part of the negative peak is mainly attributed to the bleach of the $S_0 \rightarrow S_1$ transition, as suggested by the steady state spectrum. At wavelengths longer than 650 nm the negative signal is expected to show predominantly contribution from SE, which generally follows the steady state emission spectra.

In case of Soret excitation of 3H(Phl$^{F}$) a long lived contribution (LLC) to the signal at 720 nm with strong solvent polarity dependence was observed (Fig. 4 and Fig. 5c). Assignment of this signal will require further investigations. However, its solvent polarity dependence, and its absence after Q-band excitation and in all measurements on 3H(Phl$^{CO_2H}$) suggests that it is connected to an excited state that is localized primarily on the fluorinated phenyl groups and stabilized by polar solvents. All other measurements were solvent polarity independent. For this reason measurements in toluene are shown throughout the paper except for Fig. 5c where cyclohexane was used for 720 nm detection wavelength. Since all HET measurements were performed in vacuum, measurements with a non-polar solvent were performed for comparison. Kinetic traces were measured at the probe wavelengths indicated as dashed lines in Fig. 3. Namely, 540 nm to monitor the $S_1$ and $T_1$ ESA,

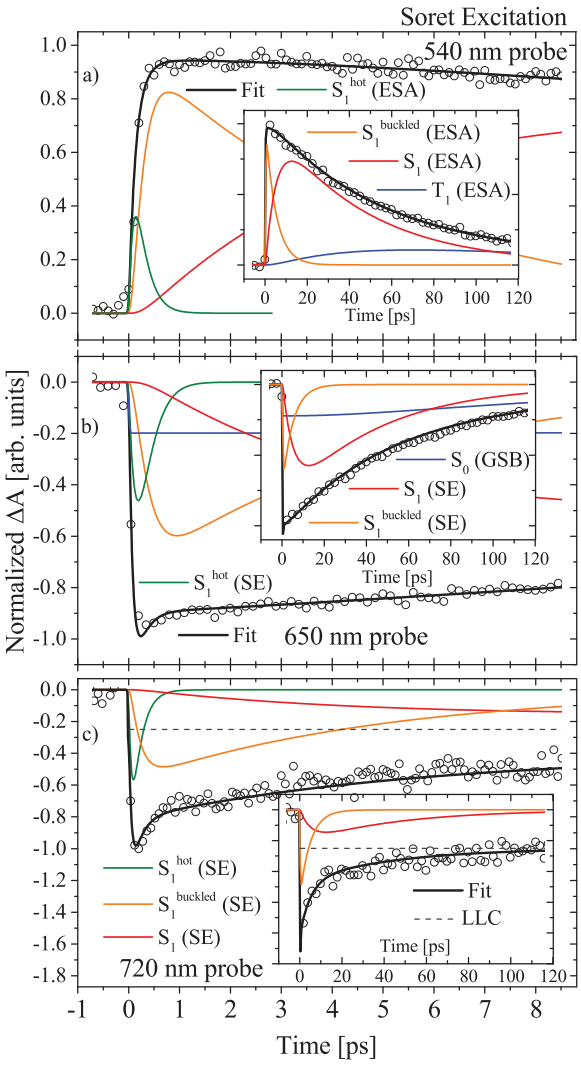


**Fig. 5** Normalized kinetic traces of 3H(Phl$^{F}$) in toluene (panel a and b) and cyclohexane (panel c) after Soret excitation. The insets show the long term behavior of the signal. Solid lines represent the fit and the contribution of each state to it. The dashed line in c) represents a long lived contribution (LLC) that is discussed in the text.

650 nm to track the GSB and SE, and 720 nm to follow the SE. These traces are shown in Fig. 5 following Soret excitation. Likewise, Fig. 6 shows the traces after Q band excitation. For the latter case traces at 650 nm were not taken due to the strong signal arising from scattered pump light.

Besides the previously mentioned long lived contribution no significant difference between 3H(Phl$^{F}$) and 3H(Phl$^{CO_2H}$) was found. Particularly during the first 9 ps the traces are indistinguishable from each other (Fig. 7). Thus, the same relaxation model, sketched in the Jablonski diagram shown in Fig. 8, was successfully used for both phlorin derivatives.

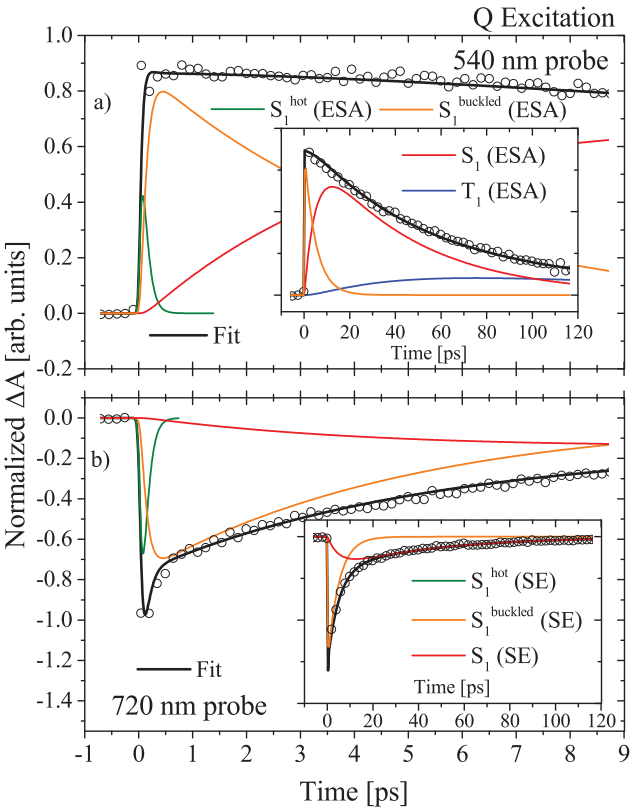


**Fig. 6** Normalized kinetic traces of 3H(PhlF) in toluene following Q band excitation. The insets show the long term behavior of the signal. Solid lines represent the fit and the contribution of each state to it.

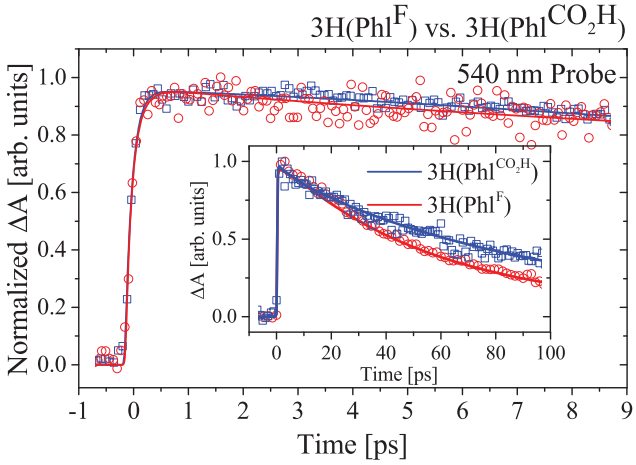


**Fig. 7** Comparison of the relaxation dynamics between 3H(PhlF) and 3H(Phl$CO_2H$) in toluene. Both systems were successfully fit with the same model.

**3.2.2 Relaxation dynamics.** To reproduce the relaxation dynamics after excitation of the Soret band, a model with 5 consecutive decay process between 6 states was required to fit all the measured traces globally. In contrast, following Q band excitation, only the last 4 process, connecting 5 of the previously identified states contribute to our signal. Assignment of the signals to individual states will be discussed next. The global fit parameters for Fig. 5 and Fig. 6 are summarized in Table 1.

*The first population* has a lifetime of ∼150 fs. Following Soret excitation, the lifetime of this state is observed as a rise at 540, 650, and 720 nm. This time constant is not observed at any wavelength following excitation of the Q band, where the $S_1$ state is populated directly. Early dynamics following excitation in the individual states are shown in Fig. 9. This state is thus identified as $S_2$, which is populated instantaneously during Soret band excitation. Its lifetime is observed as a rise time after Soret excitation in the $S_1^{hot}$ population (see below). The measured lifetime agrees with previously reported results for free base porphyrins in solution,[9,24] as well as gas phase measurements.[29,30] The ultrafast relaxation from $S_2$ to $S_1$ indicates relaxation through a conical intersection.[29]

*The second state* is identified as a vibrational hot $S_1$ species, denoted $S_1^{hot}$, with a lifetime of $\tau_2 \sim 180$ fs after Soret excitation. This time-constant is only observed in the SE signal $S_1 \rightarrow S_0$ as a decay. In contrast, the $S_1 \rightarrow S_n$ transition can in principle always access a corresponding vibrational level in the upper excited state $S_n$, and thus, the dynamics of the $S_1^{hot}$ relaxation process is not observed at 540 nm. This is indicated in Fig. 8 by the green and maroon arrows. The dynamics associated with the $S_1^{hot}$ state appear as a decay with a small amplitude at 650 nm on top of the bleach signal, along with a decay at 720 nm (green line in Fig. 5 and Fig. 6). The lifetime of this state after Q band excitation is $\tau_2' \sim 90$ fs, shown in Fig. 9. The reduced lifetime after Q band excitation can be attributed to the reduced amount of excess vibrational energy.

**Table 1** Summary of time constants ($\tau_i$) and amplitudes ($A_i^\lambda$) corresponding to the transient absorption kinetics of 3H(PhlF) in nonpolar solvent. EB: excited band, PR: probe

| EB | PB [nm] | $A_1^\lambda$ $S_2$ | $A_2^\lambda$ $S_1^{hot}$ | $A_3^\lambda$ $S_1^{buckled}$ | $A_4^\lambda$ $S_1$ | $A_5^\lambda$ $T_1$ | $A_0^\lambda$ $S_0$ |
|---|---|---|---|---|---|---|---|
| Soret | 540 | 0 | 0.26 | 0.33 | 0.32 | 0.09 | 0 |
| | 650 | 0 | -0.44 | -0.23 | -0.25 | 0 | 0.08 |
| | 720 | 0 | -0.56 | -0.32 | -0.12 | 0 | 0 |
| Q | 540 | 0 | 0.33 | 0.30 | 0.30 | 0.07 | 0 |
| | 720 | 0 | -0.62 | -0.30 | -0.08 | 0 | 0 |
| Time [ps] constants | | $\tau_1$ 0.15 | $\tau_2^a$ 0.18 | $\tau_3$ 5 | $\tau_4$ 44 | $\tau_5$ >120 | [b] |

[a] This time constant is reduced to 0.09 ps for Q band excitation.
[b] The ground state is repopulated with the triplet lifetime.

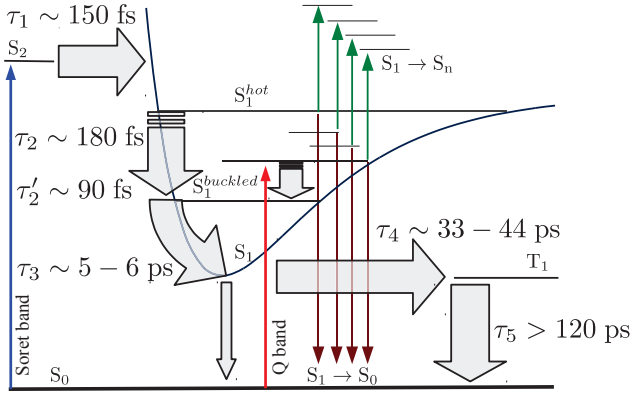


**Fig. 8** Relaxation model for the phlorins after Soret and Q band excitation.

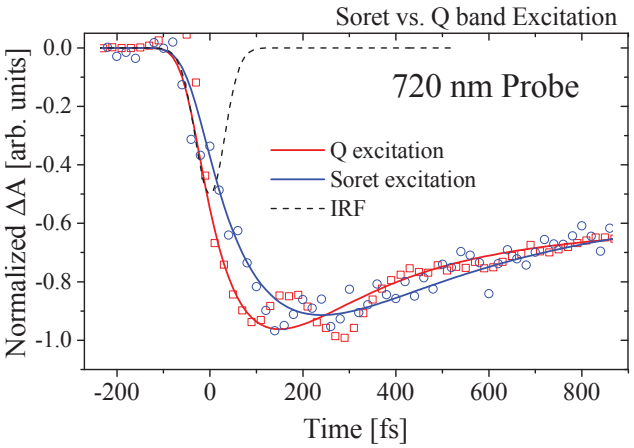


**Fig. 9** Early dynamics after excitation of the Q and Soret bands of 3H(Phl$^F$) in toluene.

This time constant is similar to those assigned to vibrational cooling processes within the Q bands of other porphyrins.[9,24]

*The third state*, with a lifetime around 6 ps, is assigned to an intermediate step in the relaxation of the Q band. This state dominates the dynamics of the SE signal at 720 nm (orange line in Fig. 5 and Fig. 6). The lifetime of this state was not affected by changing the excitation wavelength, and hence conventional vibrational cooling can be excluded. Processes with similar dynamics have been observed in other porphyrins[9,24,31,32] and have been assigned to either solvent-induced vibrational energy redistribution,[9] or to conformational changes in the relaxation pathway of non-planar porphyrins.[31,32] It is known that conformational relaxations can be sensitive to solvent polarity[33] due to the difference in polarity between the two states. A change of ~40% in the lifetime of the state was measured when using protic (methanol) as well as aprotic (DMF) polar solvents when compared to non-polar solvents (cyclohexane). In addition, molecular orbital

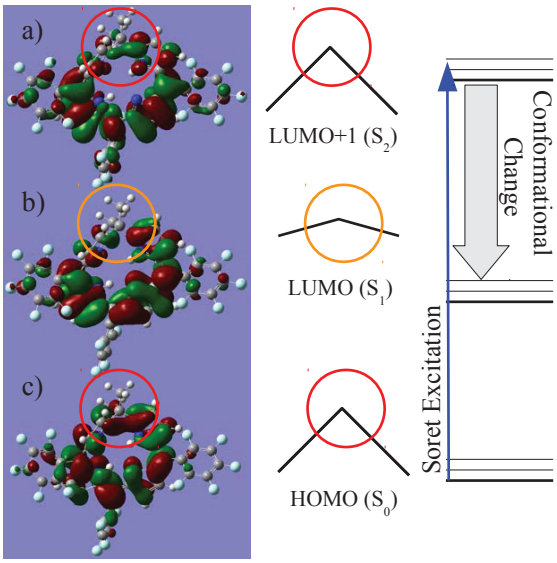


**Fig. 10** Calculated molecular orbitals for the HOMO, LUMO, and LUMO+1 of 3H(Phl$^F$) and proposed change in the conformation around the meso carbon. Notice the missing bridging orbital across the sp$^3$ hybridized *meso*-carbon in the LUMO.

calculations of 3H(Phl$^F$), depicted in Fig. 10, show that the $S_1$ state has a node at the sp$^3$ hybridized *meso*-carbon in contrast to the $S_0$ and $S_2$ states. This together with the measured buckling at the *meso*-carbon in the phlorin ground state, suggests that the geometry of the $S_1$ state differs from that of the $S_0$ and $S_2$ states. Therefore, a conformational relaxation process in the $S_1$ state is proposed. This process is thus assigned to a conformational change in the macrocycle of the phlorin, and the corresponding state is labeled $S_1^{buckled}$.

*The fourth state* corresponds to the bottom of the Q band and has a lifetime of 32 to 44 ps depending on the solvent being used. This lifetime is assigned to $S_1 \rightarrow T_1$ intersystem crossing (ISC), corresponding to the fluorescence lifetime of the molecule. Efficient ISC in free base porphyrins has been observed previously.[34,35] In addition, the time constant is in agreement with previously reported fluorescence lifetime measurements of 3H(Phl$^F$) by picosecond transient fluorescence measurements.[7] Population of this state appears as an absorption at 550 nm, as well as a negative signal at 650 and 720 nm. Contribution of this state to the fits is indicated by the red line in Fig. 5 and Fig. 6.

*Finally, the fifth state* is assigned to the triplet state $T_1$ with a lifetime longer than 120 ps exceeding the temporal detection window of our experiment. This state is assumed to decay to the ground state with a time constant corresponding to the phosphorescence lifetime, which in the case of free base porphyrins is characterized by a very low quantum yield.[34–36] Population of this state shows up as an absorption at 540 nm,

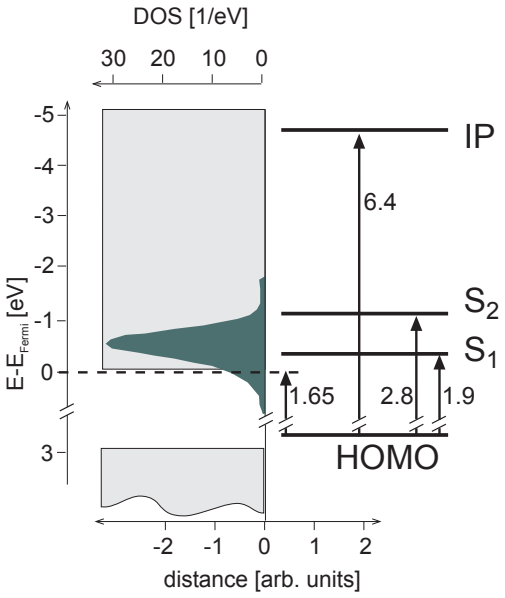


**Fig. 11** Band alignment of anatase $TiO_2$ and 3H($Phl^{CO_2H}$). All energies are given in eV. The dark gray area represents the calculated DOS for anatase (101) reproduced from Ref.[37].

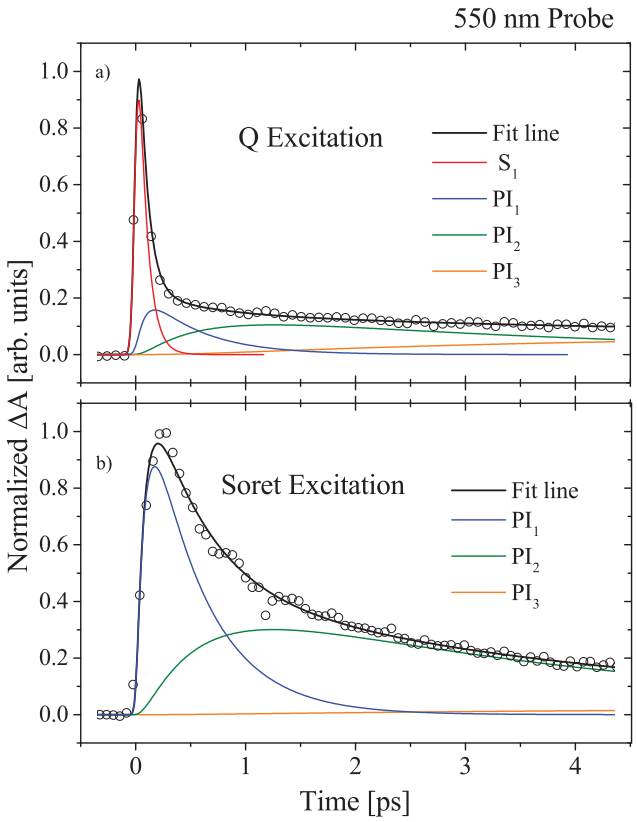


**Fig. 12** Kinetic traces of $TiO_2$ sensitized with 3H($Phl^{CO_2H}$) after Q and Soret excitation.

and its lifetime governs the GSB recovery at 650 nm. This is in agreement with reported triplet state absorption in porphyrins.[27,28] Its contribution to the fits is indicated as the blue line in Fig. 5 and Fig. 6.

### 3.3 Transient absorption of phlorin on a $TiO_2$ film.

**3.3.1 Level alignment.** Before discussing the electron injection process, it is important to know the energy band alignment between 3H($Phl^{CO_2H}$) and the $TiO_2$ film. The energy of the HOMO was calculated from the work function of anatase of 5.1 eV[38,39] and the ionization potential of free-base porphyrin of 6.4 eV[40] using results published by Lu *et al.*[41] Following their universal level alignment we can expect a HOMO to Fermi level offset of around 1.65 eV. It has been shown that the Fermi level is very close to the conduction band edge in colloidal anatase.[42] Assuming an offset of 50 meV results in a HOMO to valence band edge offset of 1.5 eV when assuming the well-established anatase band gap of 3.2 eV. This value agrees well with experimental results for a Zn-porphyrin bound to rutile $TiO_2$.[43] It should be noted that the level alignment for porphyrins does not change significantly upon substitution of side groups,[43] or removal of the central metal atom.[44] Therefore, we assume a HOMO offset of 1.65 eV for our system and deduce the position of the $S_1$ and $S_2$ state from the respective optical gaps. This results in the level alignment shown in Fig. 11. The proposed alignment has to be taken with care since changes in the surface composition can result in significant shifts. The calculated density of states (DOS) for the defect free anatase (101) surface is shown in dark gray (reproduced from Ref.[37]). It is important to note that due to the very narrow maximum of the DOS, the DOS that is resonant with the $S_1$ and $S_2$ state differs strongly independently of a systematic energy shift between the molecular states and the $TiO_2$ DOS. Assuming that the full width of the electron transfer spectrum can be accommodated inside the conduction band and that the electronic coupling between molecular excited state and $TiO_2$ acceptor states is constant over the whole energy range, it can be expected that the ET rate is proportional to the density of acceptor states. Thus, we expect a significant difference for HET times from both states.

**3.3.2 Spectroscopic properties.** Steady state absorption of the sensitized $TiO_2$ film followed closely the absorption profile of 3H($Phl^{CO_2H}$) depicted in Fig. 2. The only observed difference was a reduction in the Q band absorption. The absorption profile was measured before and after the transient absorption experiment and no appreciable changes were observed. Kinetic traces at 550, 650, and 710 nm were measured after excitation of the Soret band, and at 550, and 750 nm

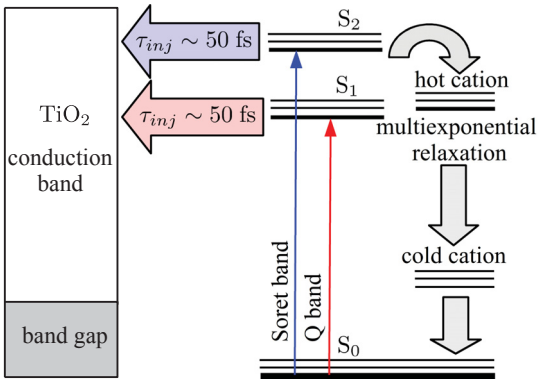


**Fig. 13** Injection model of $TiO_2$ sensitized with $3H(PhI^{CO_2H})$. The injection rate was found to be the same for Soret and Q band excitation.

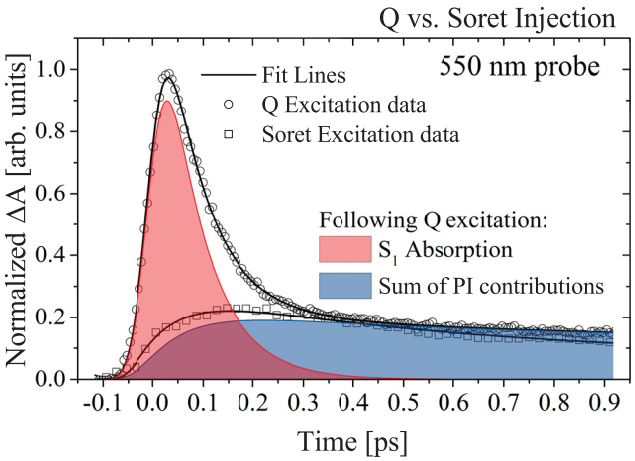


**Fig. 14** Early dynamics of electron injection process for Q and Soret excitation. The intensity is scaled at long delay times. The Soret signal can be fitted with only the contribution of post-injection species generated after Q excitation. The decay after Q band excitation (red) resembles the rise after Soret excitation (blue).

after Q band excitation. All kinetic traces show a 50±10 fs contribution. This contribution appears as the rise time of all measurements after Soret excitation, as can be seen in Fig. 12b, Fig. 15 and Fig. 16b, and is significantly faster than the $S_2 \rightarrow S_1$ transition observed in solution. After Q band excitation, the signals measured at 550 nm ($S_1$ absorption band) show a rise with the IRF followed by a fast 50 fs decay (Fig. 12a and Fig. 14). The same time constant is observed as a rise at 750 nm, identical to the dynamics measured after Soret excitation. The 50 fs process is on the same time scale as previously reported injection times for other porphyrins,[25,26,45,46] and is assigned to HET.

At later times, both Soret and Q band excited traces can be fit with the same time constants throughout the whole probe spectrum. These process have lifetimes of 0.5, 3.8 and >300 ps, and can be attributed to cation relaxation and electron recombination. The diagram showing the corresponding injection model is depicted in Fig. 13, and a summary of the parameters used for the fits is shown in Table 2.

The assignment of the different contributions to the signals is supported by the following. First, the clear correlation between the 50 fs decay and rise time of the signals after Q and Soret excitation, as well as the similarity of the dynamics after the injection process for both excitations while the $S_1$ absorption is monitored. This can be seen in Fig. 14. Second, no negative signal associated with $S_1 \rightarrow S_0$ SE was detected after Soret excitation, indicating that the $S_1$ state is not significantly populated. This is shown in Fig. 15 and Fig. 16b. In addition, traces obtained at 750 and 710 nm show the same 50 fs rise time and very similar decay dynamics after Q and Soret excitation, as can be seen in Fig. 16. The latter suggests that the two signals arise from the same post-injection states. Finally, the slow relaxation dynamics of the post-injection processes $PI_1$, $PI_2$, and $PI_3$ detected throughout the probe spectrum agree well with absorption characteristic of the cation. Cation absorption spectra have been reported for free base[47] and metal[25] porphyrins, and show a broad flat absorption between 500 nm and 750 nm. Also, long cation lifetimes up to several nanoseconds have been reported[26] in agreement with the long lived $PI_3$ contribution in our signal that can not be resolved within our temporal detection window.

These measurements show that HET proceeds with a 50 fs time constant from both states regardless of the large difference in DOS. It should be noted, that this time scale can be easily resolved with our instrument and that it is clearly different from the time constants measured for intra-molecular dynamics in solution.

**Table 2** Summary of time constants ($\tau_i$) and amplitudes ($A_i^\lambda$) corresponding to the transient absorption kinetics of $3H(PhI^{CO_2H})$ attached to $TiO_2$ displayed in Fig. 12, Fig. 15, and Fig. 16

| Excitation | Probe [nm] | $A_1^\lambda$ $S_1$ | $A_2^\lambda$ $PI_1$ | $A_3^\lambda$ $PI_2$ | $A_4^\lambda$ $PI_3$ |
|---|---|---|---|---|---|
| Soret | 550 | 0 | 0.74 | 0.24 | 0.02 |
| | 650 | 0 | 0.49 | 0.34 | 0.17 |
| | 710 | 0 | 0.42 | 0.37 | 0.21 |
| Q band | 550 | 0.79 | 0.11 | 0.07 | 0.03 |
| | 750 | 0 | 0.50 | 0.33 | 0.17 |
| Time constants [ps] | | $\tau_1$ 0.05 | $\tau_2$ 0.5 | $\tau_3$ 3.8 | $\tau_4$ >300 |

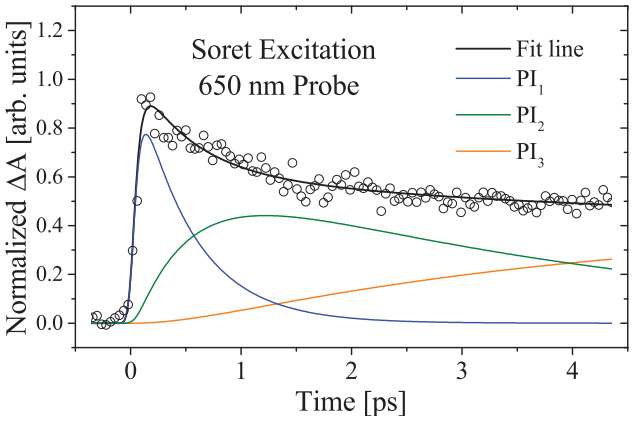


**Fig. 15** Kinetics of the sensitized film probed at 650 nm after Soret excitation.

## 4 Conclusions

We have investigated the ultrafast excited state dynamics in a novel phlorin molecule after $S_1$ and $S_2$ excitation. The overall dynamics is comparable to those reported earlier for other porphyrin derivatives. In addition to $S_2 \rightarrow S_1$ internal conversion and initial vibrational relaxation on the sub-200 fs time scale we observed a reorganization of the phlorin macrocycle. This relaxation involving the phlorin $sp^3$ hybridized meso-carbon can be ascribed to bending motions, which leads to a buckling of the porphyrin ring. ISC in this strongly fuorinated phlorin is very efficient when compared to unsubstituted porphyrins due to the heavy atom effect of the fluorine atoms.

The aforementioned dynamics measured in solvent environment changes dramatically when the phlorin molecule is attached to colloidal $TiO_2$ via a carboxylic acid anchor group. HET with a time constant around 50 fs competes with intramolecular relaxation pathways and results in the formation of the phlorin cation.

In contrast to the expected significant change in HET dynamics between the $S_1$ and $S_2$ state due to the difference in DOS, we observed identical dynamics for electron transfer from both states. This can be explained either by assuming that the DOS does not have major influence on HET, or that the assumption that the coupling between donor and acceptor state is energy independent is wrong. In the latter case the difference in DOS could in principle be compensated by stronger coupling for the $S_2$ state. However, since this explanation would require a fine balance between two uncorrelated quantities it is less likely. HET dynamics that is independent of DOS on the other hand would suggest that the first step of ET, *i.e.* the formation of the cation, involves states that are different from the surface DOS for bare $TiO_2$. The involvement of such intermediate states has been proposed earlier, mostly with regard to defect states. However, the very high efficiency

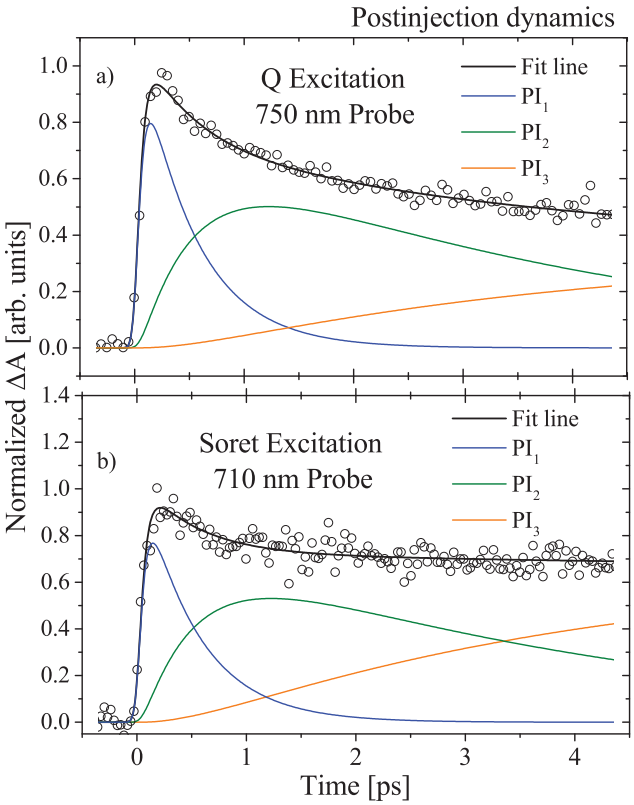


**Fig. 16** Kinetics of the sensitized film probed outside the $S_1$ absorption band. Notice the similarity of the signals after both excitations.

of initial injection quantum yield in dye/$TiO_2$ systems used for DSSC[48] suggests that these intermediate states are inherently present in the system and may better be characterized as transition states that are not observed in the DOS obtained from calculations or steady state measurements. Transient spectra of the molecular moiety of a HET system do not give the full picture for charge separation in HET. Two-photon photoelectron spectroscopy would be one way to perform complementary measurements that allow for the dynamics of electrons after HET in the conduction band to be elucidated.[49]

## Acknowledgements

J.R. thanks the NSF for support through CAREER award CHE-1352120.

## References

1 N. T. La Porte, D. B. Moravec and M. D. Hopkins, *Proceedings of the National Academy of Sciences*, 2014, **111**, 9745–9750.

2 O. Morawski, K. Izdebska, E. Karpiuk, J. Nowacki, A. Suchocki and A. L. Sobolewski, *Phys. Chem. Chem. Phys.*, 2014, **16**, 15256–15262.

3 D. Feng, W.-C. Chung, Z. Wei, Z.-Y. Gu, H.-L. Jiang, Y.-P. Chen, D. J. Darensbourg and H.-C. Zhou, *Journal of the American Chemical Society*, 2013, **135**, 17105–17110.

4 J. Lu, B. Zhang, H. Yuan, X. Xu, K. Cao, J. Cui, S. Liu, Y. Shen, Y. Cheng, J. Xu and M. Wang, *The Journal of Physical Chemistry C*, 2014, **118**, 14739–14748.

5 S. Ye, A. Kathiravan, H. Hayashi, Y. Tong, Y. Infahsaeng, P. Chabera, T. Pascher, A. P. Yartsev, S. Isoda, H. Imahori and V. Sundström, *The Journal of Physical Chemistry C*, 2013, **117**, 6066–6080.

6 A. S. Hart, B. K. Chandra, H. B. Gobeze, L. R. Sequeira and F. D'Souza, *ACS Applied Materials & Interfaces*, 2013, **5**, 5314–5323.

7 A. J. Pistner, D. A. Lutterman, M. J. Ghidiu, Y.-Z. Ma and J. Rosenthal, *Journal of the American Chemical Society*, 2013, **135**, 6601–6607.

8 A. J. Pistner, D. A. Lutterman, M. J. Ghidiu, E. Walker, G. P. A. Yap and J. Rosenthal, *The Journal of Physical Chemistry C*, 2014, **118**, 14124–14132.

9 J. S. Baskin, H.-Z. Yu and A. H. Zewail, *The Journal of Physical Chemistry A*, 2002, **106**, 9837–9844.

10 H.-Z. Yu, J. S. Baskin and A. H. Zewail, *The Journal of Physical Chemistry A*, 2002, **106**, 9845–9854.

11 M. Kullmann, A. Hipke, P. Nuernberger, T. Bruhn, D. C. G. Gotz, M. Sekita, D. M. Guldi, G. Bringmann and T. Brixner, *Phys. Chem. Chem. Phys.*, 2012, **14**, 8038–8050.

12 M. R. di Nunzio, B. Cohen, S. Pandey, S. Hayse, G. Piani and A. Douhal, *The Journal of Physical Chemistry C*, 2014, **118**, 11365–11376.

13 D. Sharma, G. Steen, J. P. Korterik, M. Garcìa-Iglesias, P. Vàzquez, T. Torres, J. L. Herek and A. Huijser, *The Journal of Physical Chemistry C*, 2013, **117**, 25397–25404.

14 R. Berera, R. van Grondelle and J. Kennis, *Photosynthesis Research*, 2009, **101**, 105–118.

15 U. Megerle, I. Pugliesi, C. Schriever, C. Sailer and E. Riedle, *Applied Physics B*, 2009, **96**, 215–231.

16 L. Gundlach, R. Ernstorfer, E. Riedle, R. Eichberger and F. Willig, *Applied Physics B*, 2005, **80**, 727–731.

17 V. I. Klimov and D. W. McBranch, *Opt. Lett.*, 1998, **23**, 277–279.

18 A. J. Pistner, G. P. A. Yap and J. Rosenthal, *The Journal of Physical Chemistry C*, 2012, **116**, 16918–16924.

19 J. Rochford, D. Chu, A. Hagfeldt and E. Galoppini, *Journal of the American Chemical Society*, 2007, **129**, 4655–4665.

20 R. Ernstorfer, *PhD thesis*, Freie Universität Berlin, 2004.

21 T. D. LeSaulnier, B. W. Graham and G. R. Geier III, *Tetrahedron Letters*, 2005, **46**, 5633 – 5637.

22 M. Gouterman, G. H. Wagnière and L. C. Snyder, *Journal of Molecular Spectroscopy*, 1963, **11**, 108 – 127.

23 N. B. Neto, D. Correa, L. D. Boni, G. Parra, L. Misoguti, C. Mendonça, I. Borissevitch, S. Zlio and P. Gonçalves, *Chemical Physics Letters*, 2013, **587**, 118 – 123.

24 M. Enescu, K. Steenkeste, F. Tfibel and M.-P. Fontaine-Aupart, *Phys. Chem. Chem. Phys.*, 2002, **4**, 6092–6099.

25 C.-W. Chang, L. Luo, C.-K. Chou, C.-F. Lo, C.-Y. Lin, C.-S. Hung, Y.-P. Lee and E. W.-G. Diau, *The Journal of Physical Chemistry C*, 2009, **113**, 11524–11531.

26 H. Imahori, S. Kang, H. Hayashi, M. Haruta, H. Kurata, S. Isoda, S. E. Canton, Y. Infahsaeng, A. Kathiravan, T. Pascher, P. Chabera, A. P. Yartsev and V. Sundstrom, *The Journal of Physical Chemistry A*, 2011, **115**, 3679–3690.

27 M. Gouterman, *The Journal of Chemical Physics*, 1960, **33**, 1523–1529.

28 A. Harriman, *J. Chem. Soc., Faraday Trans. 2*, 1981, **77**, 1281–1291.

29 M.-H. Ha-Thi, N. Shafizadeh, L. Poisson and B. Soep, *Phys. Chem. Chem. Phys.*, 2010, **12**, 14985–14993.

30 M.-H. Ha-Thi, N. Shafizadeh, L. Poisson and B. Soep, *The Journal of Physical Chemistry A*, 2013, **117**, 8111–8118.

31 S. Gentemann, C. J. Medforth, T. Ema, N. Y. Nelson, K. M. Smith, J. Fajer and D. Holten, *Chemical Physics Letters*, 1995, **245**, 441 – 447.

32 J. L. Retsek, S. Gentemann, C. J. Medforth, K. M. Smith, V. S. Chirvony, J. Fajer and D. Holten, *The Journal of Physical Chemistry B*, 2000, **104**, 6690–6693.

33 F. J. Vergeldt, R. B. M. Koehorst, A. van Hoek and T. J. Schaafsma, *The Journal of Physical Chemistry*, 1995, **99**, 4397–4405.

34 S. Perun, J. Tatchen and C. M. Marian, *ChemPhysChem*, 2008, **9**, 282–292.

35 A. T. Gradyushko and M. P. Tsvirko, *Opt. Spectrosk.*, 1971, **31**, 291.

36 M. P. Tsvirko, K. N. Solovjev, A. T. Gradyushko and S. S. Dvornikov, *Opt. Spectrosk.*, 1975, **38**, 400.

37 X. Zhang, Q. Chen, J. Tang, W. Hu and J. Zhang, *Sci. Rep.*, 2014, **4**, 4762–(11).

38 D. O. Scanlon, C. W. Dunnill, J. Buckeridge, S. A. Shevlin, A. J. Logsdail, S. M. Woodley, C. R. A. Catlow, M. J. Powell, R. G. Palgrave, I. P. Parkin, G. W. Watson, T. W. Keal, P. Sherwood, A. Walsh and A. A. Sokol, *Nature Materials*, 2013, **12**, 798–801.

39 G. Xiong, R. Shao, T. Droubay, A. Joly, K. Beck, S. Chambers and W. Hess, *Advanced Functional Materials*, 2007, **17**, 2133–2138.

40 D. P. Piet, D. Danovich, H. Zuilhof and E. J. R. Sudholter, *J. Chem. Soc., Perkin Trans. 2*, 1999, 1653–1662.

41 M. T. Greiner, M. G. Helander, T. Wing-Man, W. Zhi-Bin, Q. Jacky and L. Zheng-Hong, *Nat. Mater.*, 2012, **11**, 76–81.

42 R. Ernstorfer, L. Gundlach, S. Felber, W. Storck, R. Eichberger and F. Willig, *The Journal of Physical Chemistry*, 2006, **110**, 25383–25391.

43 S. Rangan, S. Coh, R. A. Bartynski, K. P. Chitre, E. Galoppini, C. Jaye and D. Fischer, *The Journal of Physical Chemistry C*, 2012, **116**, 23921–23930.

44 K. B. Ornso, C. S. Pedersen, J. M. Garcia-Lastra and K. S. Thygesen, *Phys. Chem. Chem. Phys.*, 2014, **16**, 16246–16254.

45 L. Luo, C.-F. Lo, C.-Y. Lin, I.-J. Chang and E. W.-G. Diau, *The Journal of Physical Chemistry B*, 2006, **110**, 410–419.

46 G. Ramakrishna, S. Verma, D. A. Jose, D. K. Kumar, A. Das, D. K. Palit and H. N. Ghosh, *The Journal of Physical Chemistry B*, 2006, **110**, 9012–9021.

47 E. A. Alemán, J. Manríquez Rocha, W. Wongwitwichote, L. A. Godínez Mora-Tovar and D. A. Modarelli, *The Journal of Physical Chemistry A*, 2011, **115**, 6456–6471.

48 A. Listorti, B. O'Regan and J. R. Durrant, *Chemistry of Materials*, 2011, **23**, 3381–3399.

49 L. Gundlach, R. Ernstorfer and F. Willig, *Applied Physics A*, 2007, **88**, 481–495.